Structure Dynamics of Carbon-Supported Platinum-Neodymium Nanoalloys during the Oxygen Reduction Reaction

Carlos Campos-Roldán, Raphaël Chattot, Jean-Sébastien Filhol, Hazar Guesmi, Frédéric Pailloux, Rémi Bacabe, Pierre-Yves Blanchard, Andrea Zitolo, Jakub Drnec, Deborah Jones, et al.

▶ **To cite this version:**

Carlos Campos-Roldán, Raphaël Chattot, Jean-Sébastien Filhol, Hazar Guesmi, Frédéric Pailloux, et al.. Structure Dynamics of Carbon-Supported Platinum-Neodymium Nanoalloys during the Oxygen Reduction Reaction. ACS Catalysis, 2023, 13 (11), pp.7417-7427. 10.1021/acscatal.3c00371 . hal-04156475

HAL Id: hal-04156475
https://hal.science/hal-04156475

Submitted on 8 Jul 2023

HAL is a multi-disciplinary open access archive for the deposit and dissemination of scientific research documents, whether they are published or not. The documents may come from teaching and research institutions in France or abroad, or from public or private research centers.

L'archive ouverte pluridisciplinaire **HAL**, est destinée au dépôt et à la diffusion de documents scientifiques de niveau recherche, publiés ou non, émanant des établissements d'enseignement et de recherche français ou étrangers, des laboratoires publics ou privés.

Structure Dynamics of Carbon-Supported Platinum-Neodymium Nanoalloys during the Oxygen Reduction Reaction

*Carlos A. Campos-Roldán†, Raphaël Chattot†, Jean-Sébastien Filhol,† Hazar Guesmi,† Frédéric Pailloux‡, Rémi Bacabe,† Pierre-Yves Blanchard†, Andrea Zitolo,¶ Jakub Drnec,ɖ Deborah J. Jones†, Sara Cavaliere †**

† ICGM, Univ. Montpellier, CNRS, ENSCM, 34095 Montpellier cedex 5, France

‡ Institut P', CNRS - Université de Poitiers – ISAE-ENSMA - UPR 3346, 11 Boulevard Marie et Pierre Curie, Site du Futuroscope, TSA 41123, 86073 Poitiers cédex 9, France

¶ Synchrotron SOLEIL, L'Orme des Merisiers, BP 48 Saint Aubin, 91192 Gif-sur-Yvette, France

ɖ ESRF, European Synchrotron Radiation Facility, 71 Avenue des Martyrs, CS40220, 38043 Grenoble Cedex 9, France

*Corresponding author: sara.cavaliere@umontpellier.fr

KEYWORDS: Pt alloys, Rare Earth Metals, Operando measurements, Oxygen Reduction Reaction, Proton Exchange Membrane Fuel cells.

ABSTRACT

Platinum-rare earth nanoalloys have been predicted to be promising proton exchange membrane fuel cell (PEMFC) electrocatalysts for the cathodic oxygen reduction reaction (ORR). However, their implementation in PEMFCs is limited by the challenge of their preparation as carbon-supported nanostructures. Consequently, the practical structure-activity-stability trends for this class of nanoalloys remain largely unexplored. Herein, carbon-supported Pt-Nd nanoalloys as ORR electrocatalysts are described. The physical chemistry of selected electrocatalysts was extensively investigated by means of combined *ex situ* and *operando* techniques, which reveal the unique structural dynamics of Pt-Nd nanoalloys in a simulated PEMFC cathode environment. The experimental observations, supported by theoretical calculations, indicate that after initial significant structural modification in the early stage of operation, the ORR activity is mediated in the longer-term by surface compressive strain rather than charge transfer between Pt and Nd. Such key *operando* structure-activity-stability relations underpin further optimization of carbon-supported Pt-rare earth nanoalloys as fuel cell cathode catalysts.

1. INTRODUCTION

Proton-exchange membrane fuel cells (PEMFCs) are considered as suitable devices to contribute to the CO_2 neutrality targets,[1] and have gained much attention for use in heavy-duty and long-distance transportation due to the high gravimetric energy density of hydrogen.[2] Notwithstanding, the massive implementation of PEMFCs is still hindered by technical barriers that need to be overcome, including performance, durability, cost and fuel efficiency.[3, 4] In fact, the performance of a PEMFC has an important dependency on the catalyst layers,[5] which usually possess high Pt

loadings specially at the cathode, where the sluggish oxygen reduction reaction (ORR) takes place. Therefore, tailoring high-performance Pt-based electrocatalysts for the ORR is of paramount importance, which current target is to use 0.1 g_{PGM}/kW (platinum-group metal, PGM) for automotive and 0.3 g_{PGM}/kW for heavy-duty transport applications.[2]

A widely used strategy to increase the activity of ORR electrocatalysts is by alloying Pt with late transition metals (usually Ni, Co, Fe, Cu, *etc*), which also decreases simultaneously the amount of Pt.[5] However, the long-term stability of these materials represents a crucial issue that must be overcome.[6, 7] In this context, Pt-rare earth metal (Pt-REM) alloys have been proposed as a promising family of highly active/stable electrocatalysts for the ORR.[8] Theoretical studies suggested that the exceptionally negative formation energy of Pt-REM alloys represents a kinetic barrier to diffusion of the REM atom, and impedes the alloy degradation.[8, 9] Experimental evidence with bulk sputter-cleaned polycrystalline electrodes[10-13] and unsupported nanoparticles (NPs)[14, 15] revealed that the high activity of these alloys (including the cubic structure Pt_3Y system) stems from the formation of a specific structure, in which the Pt-REM alloy is protected by a Pt-rich overlayer,[16] which experiences a lateral compressive strain.[11, 16] Indeed, the surface specific ORR activity showed an exponential dependence on the degree of compressive strain in the Pt-REM alloys.[14, 15]

Escudero-Escribano *et al.*[13] correlated the ORR specific activity of Pt_5REM sputter-cleaned polycrystalline electrodes (REM = La, Ce, Sm, Gd, Tb, Dy, Tm) to the *ex situ* measured Pt lattice parameter. Pt_5REM forms a hexagonal crystalline structure, the atomic arrangement of which

stabilizes the so-called *kagome* layer.[16] This particular configuration presents an unusual $CaCu_5$-like structure that accommodates the alloying elements of different atomic radius in a different way from face centered cubic (FCC) or hexagonal close packed (HCP) alloys, to form uniform bond lengths between Pt-Pt, Pt-REM and REM-REM:[16] the $CaCu_5$ structure consists of alternating layers of Pt_2REM and Pt_3 layers. The pure Pt layers in bulk Pt_5M alloys have hollow vacancy-like spaces at positions below and above the REM atoms. This results in a compressed Pt overlayer despite alloying Pt with larger REM atoms, which can be explained by the hexagonal symmetry of both the Pt(111) surface and the Pt_5REM bulk structure. In fact, the lattice parameter *a* in the hexagonal structure continues its contraction while moving towards the so-called lanthanide contraction, but the *b* and *c* lattice parameters are considerably different due to the different re-organization of the atoms. Namely, for Pt-REM alloys with the $CaCu_5$-like structure, the unit cell *a* will contract (shorter Pt-Pt distances) as the REM covalent radii decreases (lanthanide contraction).[13] *Ex situ* measurements of the imposed compressive strain in the Pt lattice revealed that the specific ORR activity is highest at a contraction of -3 %, respect to Pt bulk.[13]

Nevertheless, the limited availability of carbon-supported Pt-REM nanostructures has restricted the transposition of the results obtained on model extended surfaces to practical PEMFCs. Indeed, synthesis of nanoparticle Pt-REM alloys is challenging due to the highly negative standard redox potential of rare earth metals (far beyond the stability range of water) and their high oxophilicity, which favours formation of REM oxygen-containing species instead of alloys.[17] Although recent synthesis approaches[17-20] have enabled the preparation of carbon-supported Pt-REM nanoalloys, their reported ORR mass activity (between 0.3 - 0.7 A mg_{Pt}^{-1})[21-23] is far below that of unsupported

9 nm Pt_xY[14] NPs (3.05 A mg_{Pt}^{-1}) or 8 nm Pt_xGd[15] NPs (3.60 A mg_{Pt}^{-1}). Therefore, further understanding and optimization of Pt-REM/C nanoalloys are still needed.

In situ and/or *operando* techniques, such as X-ray diffraction (XRD), X-ray absorption spectroscopy (XAS), *online* inductively coupled plasma mass spectrometry (ICP-MS), *etc*., are essential tools to understand electrocatalyst behaviour in real or simulated electrochemical environments of the application device. Indeed, it is largely accepted that fundamental reactivity descriptors (*e.g.* surface strain, chemistry and/or crystallinity) of Pt-based electrocatalysts measured and tailored *ex situ* are not necessarily conserved *in situ*[24-27] due to surface reconstruction in the particular environment of the PEMFC cathode on operation.[24, 28] Indeed, to the best of our knowledge, such *In situ* and/or *operando* techniques has never been used to investigate this promising novel class of Pt-REM/C nanoalloys.

In this contribution, we describe the synthesis and extensive characterization of carbon-supported Pt-Nd nanoalloys. By adjusting the quantity of the Nd chemical precursor during the synthesis, the Pt:Nd composition in the final electrocatalyst was systematically modulated and the ORR activity was tailored. Two Pt-Nd/C electrocatalysts of different crystal structure were selected on the basis of their high ORR activity, and were investigated by means of an extensive range of combined *ex situ* (WAXS, XAS, HRTEM, STEM/EELS, ICP-MS) and *operando* (WAXS) techniques. The *ex situ* and *operando* structural properties of the selected materials were rationalized and compared, to shed new light on the *operando* structure-activity-stability relationships of carbon-supported Pt-REM nanoalloys.

3. RESULTS AND DISCUSSION

We have prepared Pt-Nd/C nanoalloys using the carbodiimide complex route proposed by Hu *et al.*[18] with some modifications[29, 30] (see Supplementary Information S1). Firstly, five Pt:Nd atomic ratios (16.5:1, 7.8:1, 6.1:1, 5.7:1 and 5.4:1) were obtained by systematically varying the Nd precursor content in the synthesis. The Pt_xNd/C catalyst series prepared was subsequently characterized by means of XRD, ICP-MS and electron microscopy, and their electrocatalytic activity was investigated using the RDE technique in 0.1 M $HClO_4$ electrolyte (see Supplementary Information S6). This preliminary screening revealed that the $Pt_{7.8}Nd/C$ and $Pt_{6.1}Nd/C$ electrocatalysts present the highest activity for the ORR among the series (0.55 A mg_{Pt}^{-1} and 0.63 A mg_{Pt}^{-1} at 0.9 V_{RHE}, respectively), surpassing the reference Pt/C material from Johnson-Matthey (0.24 A mg_{Pt}^{-1}). Interestingly, and despite relatively close overall chemical composition and ORR activity, the crystalline structures of these two materials revealed by XRD are different, with $Pt_{6.1}Nd/C$ presenting only the Pt_5Nd hexagonal phase and $Pt_{7.8}Nd/C$ a mixture of cubic Pt, cubic Pt_2Nd and hexagonal Pt_5Nd phases. These two electrocatalysts were selected as model samples for a more comprehensive understanding of the structure-activity-stability trends in this class of nanoalloys.

Rietveld full profile refinement of the wide-angle synchrotron X-ray scattering (WAXS) patterns of $Pt_{7.8}Nd/C$ and $Pt_{6.1}Nd/C$ collected *ex situ*, see Figure 1a, confirms the above results obtained from laboratory-source XRD. Quantitative phase analysis indicates that the $Pt_{7.8}Nd/C$ sample comprises 51 *wt.%* hexagonal Pt_5Nd, 37 *wt.%* FCC Pt and 12 *wt.%* cubic Pt_2Nd crystalline phases, and that the $Pt_{6.1}Nd/C$ sample is 100 *wt.%* hexagonal Pt_5Nd crystal structure. Further

microstructural parameters, such as the lattice constants of these phases and their associated coherent domain sizes, were extracted from the Rietveld refinement, and are shown in Table 1. Compared to the reference Pt/C electrocatalyst, the nearest neighbour Pt-Pt distances are shorter in the Pt_2Nd and Pt_5Nd crystalline arrangements, corresponding to a compressive strain of *ca.* -2% and -3%, respectively.

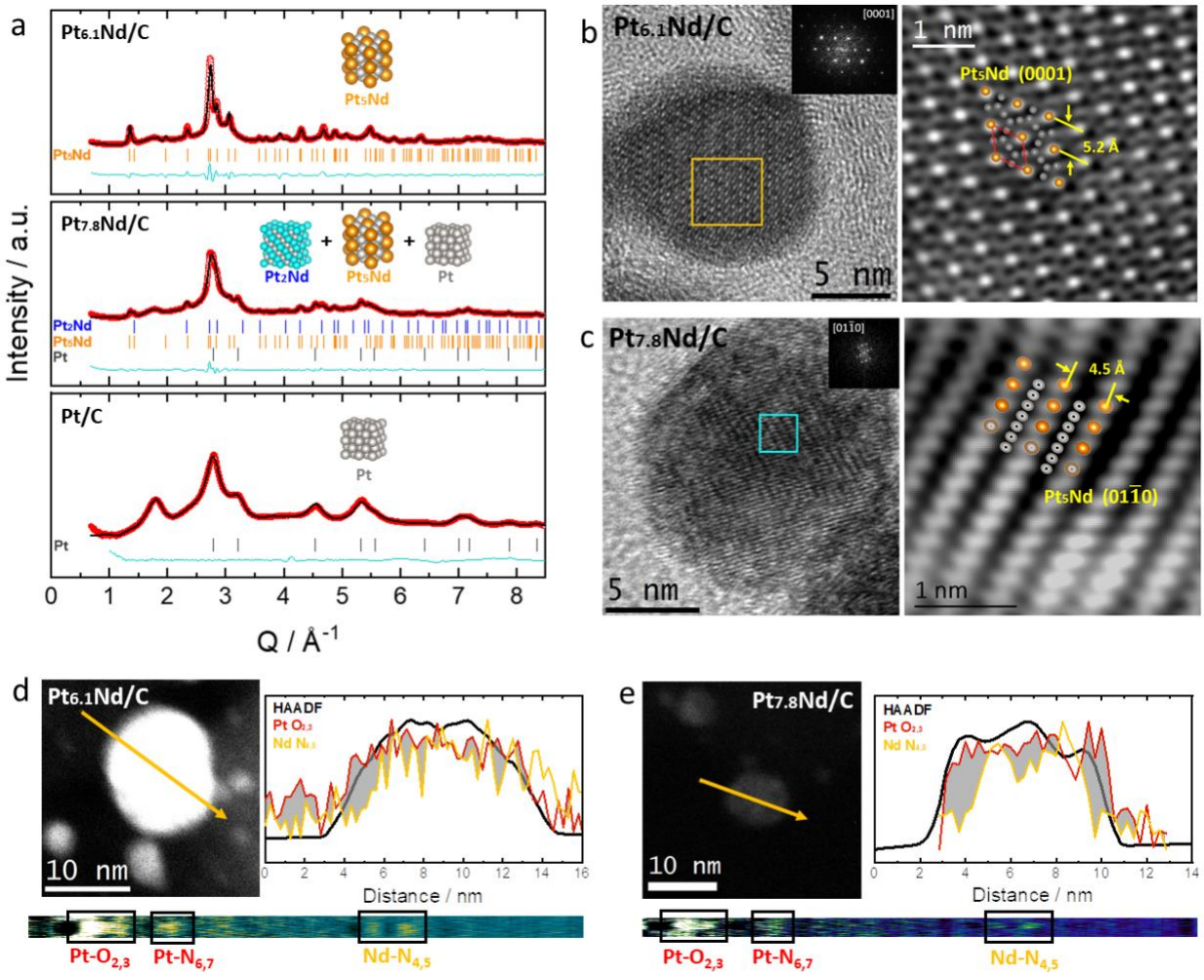

Figure 1. (a) Refined *ex situ* WAXS patterns (vertical bars represent the theoretical diffraction pattern of each crystalline phase, and the cyan line represents the residual from the refinement); representative HRTEM micrographs of (b) $Pt_{6.1}Nd/C$ and (c) $Pt_{7.8}Nd/C$; and (c) representative HAADF-STEM/EELS analysis of (d) $Pt_{6.1}Nd/C$ and (e) $Pt_{7.8}Nd/C$. Pt/C is used as reference in (a).

Table 1. Chemical composition, particle size and refined structural data of $Pt_{6.1}Nd/C$ and $Pt_{7.8}Nd/C$. Pt/C is used as reference.

	[a] Metal content (%wt.)	[a] Pt:Nd ratio	[b] Mean particle size (nm)	Crystalline phase weight fraction (%)	Lattice parameter *a* (Å)	[c] Lattice parameter *c* (Å)	Coherent domain size (nm)	Pt – Pt distance (Å)	[d] ε (%)
$Pt_{7.8}Nd/C$	Pt: 26.67 Nd: 2.52	7.8 : 1	6.1 ± 1.6 *12.8 ± 1.7	Pt_5Nd: 51 Pt_2Nd: 12 Pt: 37	Pt_5Nd: 5.357 Pt_2Nd: 7.644 Pt: 3.914	Pt_5Nd: 4.421	Pt_5Nd: 4.0 Pt_2Nd: 5.3 Pt: 3.2	Pt_5Nd: 2.678 Pt_2Nd: 2.702 Pt: 2.767	Pt_5Nd: -3.1 Pt_2Nd: -2.2 Pt: 0.1
$Pt_{6.1}Nd/C$	Pt: 27.04 Nd: 3.29	6.1 : 1	6.8 ± 1.5 *13.1 ± 2.1	Pt_5Nd: 100	Pt_5Nd: 5.364	Pt_5Nd: 4.408	Pt_5Nd: 9.5	Pt_5Nd: 2.682	Pt_5Nd: -3.0
Pt/C	Pt: 47.2	--	3.7 ± 0.9	Pt: 100	Pt: 3.909	--	Pt: 1.6	Pt: 2.764	0

a: Determined by ICP-MS; b: Determined by TEM; c: in a hexagonal structure a=b≠c; d: Relative to Pt/C. * Average size of agglomerates.

High resolution TEM overviews and the corresponding power spectrum on isolated NPs, Figure 1b and c, resolve the atomic arrangements in both materials, where the Pt_5Nd (0001) and the Pt_5Nd $(01\bar{1}0)$ crystalline planes are observed for $Pt_{6.1}Nd/C$ and $Pt_{7.8}Nd/C$, respectively. For both electrocatalysts, the results of combined HAADF-STEM and EELS analyses, Figure 1d and 1e, also confirm the presence of both Pt and Nd in the NPs. Due to the difference between the Pt and Nd dissolution potentials and the post-synthesis acidic wash (4 h in N_2-saturated 0.5 M H_2SO_4), it is expected the stabilization of a Pt-rich shell surrounded the alloy structure.[31] Based on the computed phase diagram of the possible structures and their associated stabilities (see the Supplementary Information S9), a pure Pt monolayer over the Pt_5Nd alloy (Pt_5Nd@Pt) is a quite stable structure. Considering that the thickness of an atomic monolayer of Pt is ~ 0.2 nm, and that the probe size and the probe step in the HAADF-STEM/EELS were 0.5 nm and 0.4 nm respectively, the detection of one atomic Pt monolayer is clearly below the detection limit of the

161 microscope used. Therefore, the presence of Pt_5Nd@Pt with a thinner Pt overlayer or structures
162 with Pt-rich multilayers cannot be ruled out.

163 The near-surface composition was investigated by XPS. Figure 2a shows the Pt 4*f* photoemission
164 lines, which indicates the predominance of the Pt metallic state at the near-surface region in all
165 cases (the survey spectra and the Nd 3*d* photoemission lines are given in the Supplementary
166 Information S7). However, the binding energy position of the Pt metallic doublet in $Pt_{7.8}Nd/C$ and
167 $Pt_{6.1}Nd/C$ is downshifted with respect to that of the Pt/C reference, suggesting a modification of
168 the Pt electronic structure. The alloy formation energy ($\Delta H°_{Pt5Nd}$ = -55 kJ g^{-1} $atom^{-1}$)[32] correlates
169 with the difference in electronegativity between the alloying metals,[33] leading to charge transfer
170 from Nd (χ_{Nd}= 1.14) to Pt (χ_{Pt}= 2.28) and increased electron density around Pt. Besides,
171 compressive strain, *i.e.*, shorter Pt-Pt interatomic distances, might also modify the electronic states
172 of Pt due to the overlapping of the electron conduction bands.[34]

173

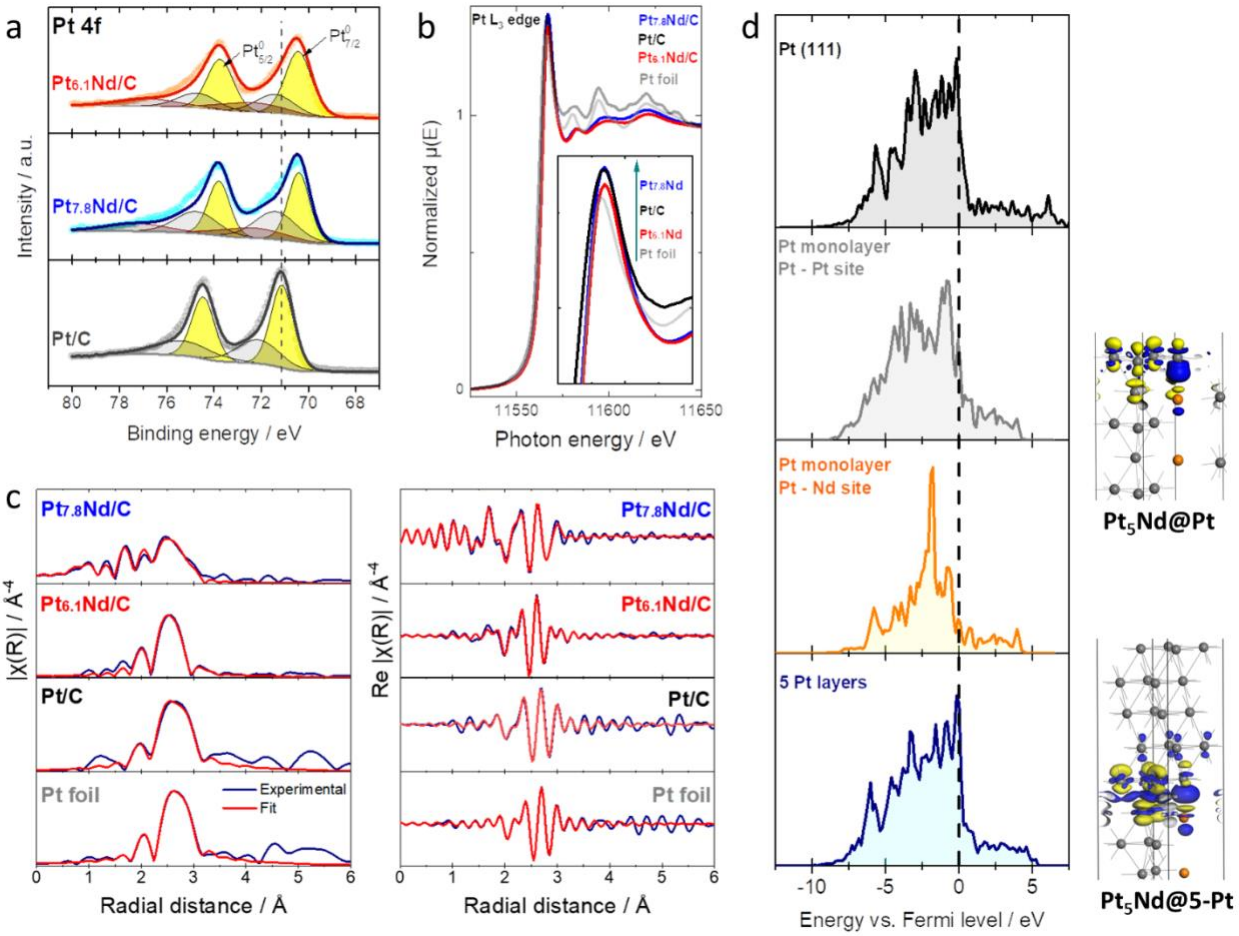

Figure 2. (a) Pt 4f photoemission lines (Pt/C is used as reference); *ex situ* Pt L_3 edge (b) XANES and (c) fitted FT EXAFS spectra (Pt foil and Pt/C are used as reference) of $Pt_{6.1}Nd/C$ and $Pt_{7.8}Nd/C$. (d) Projected density of states (PDOS) of Pt surface atoms from Pt (111) surface, $Pt_5Nd@Pt$ or $Pt_5Nd@5$-Pt. To show the effect of sub-surface Nd on the electronic structure of surface Pt in $Pt_5Nd@Pt$, the PDOS on different surface Pt atom either on top of a subsurface Nd atom or above 3 subsurface Pt atoms are represented.

The local electronic structure and coordination environment of Pt in the electrocatalysts was studied using X-ray absorption spectroscopy (XAS). The *ex situ* X-ray absorption near-edge structure (XANES) at the Pt L_3 edge are shown in Figure 2b for $Pt_{7.8}Nd/C$ and $Pt_{6.1}Nd/C$. As reference, Pt/C and the Pt foil were used. The white line intensity in the XANES spectra indicates

the transition from occupied Pt 2*p* electrons to empty Pt 5*d* states. Therefore, this parameter is indicative of the Pt 5*d* band occupancy,[24] with a higher white line intensity suggesting higher density of unoccupied valence states at Pt sites (more vacancies) respect to the Pt foil. As seen in Figure 2b, the white line intensity follows the trend Pt foil < $Pt_{6.1}Nd/C$ < Pt/C ≤ $Pt_{7.8}Nd/C$. The average first-shell Pt-Pt bond lengths were determined by fitting the filtered Fourier Transform X-ray absorption fine structure (EXAFS) spectra, shown in Figure 2c and Supplementary Information S8 respectively. The nearest neighbor Pt-Pt interatomic distances are shorter for $Pt_{6.1}Nd/C$ and $Pt_{7.8}Nd/C$ than in the reference Pt/C and Pt foil, which reflects a compressive strain of *ca.* -3 % and -1.6 % respectively, in agreement with the refined WAXS parameters.

Density functional theory (DFT) calculations were carried out to gain more information on the electronic structure of the Pt-Nd electrocatalysts. As was mentioned above, the optimization of several alloyed Pt_5Nd systems, through the calculation of their grand potential as a function of the Pt chemical potential (see details in the Supplementary Information S9), predicts the stability of a slab with a pure Pt monolayer (Pt_5Nd@Pt) and the metastability of thicker Pt-covered slabs with 5 Pt overlayers (Pt_5Nd@5-Pt), which agrees with the experimental data shown in Figure 1. Such structures are compressively strained relative to the Pt (111) reference, with shorter Pt-Pt interatomic distances in the *x*-*y* plane, of average value of 2.67 Å (2.75 Å for the Pt reference), in line with the experimental results.

Interestingly, in the Pt_5Nd@Pt structure model, the Pt atom of the monolayer just above the Nd atom appears to be electron-enriched, while Nd undergoes an electron loss (Figure 2d), suggesting

a strongly polarized bond between $Pt^{\delta-}$ and $Nd^{\delta+}$. In fact, the surface work function of Pt_5Nd@Pt (5.53 eV) is computed to be lower than that of Pt (111) (5.70 eV), which confirms electronic enrichment of the surface. This increased electron density on Pt might be reflected in the downshift observed by XPS in the Pt 4*f* region (Figure 2a). The computed projected densities of states (PDOS), *c.f.* Figure 2d, exhibits a strong narrow peak for the Pt located on top of the subsurface Nd (associated with the Pt-d_{z^2} orbital), which suggests a decrease of its orbital overlaps with the surrounding atoms, in agreement with the formation of a Pt-Nd partially ionic bond. Thus, this Pt site on Pt_5Nd@Pt has a specific reactivity between a delocalized surface and an isolated atomic structure.

In the case of the Pt_5Nd@5-Pt structure, although the Pt atoms at the interface with Pt_5Nd create similar bonding associated with a charge transfer from Nd toward the closest Pt atoms as for the case of Pt_5Nd@Pt, no significant charge transfer from Nd is found to occur beyond the two first neighboring Pt layers. However, the Pt atoms at the surface still experience compressive strain, induced by the epitaxy on the Pt_5Nd alloy. Thus, the modification of the surface electronic properties is due to an increase of the *d*-band width compared to Pt (111), which results from the stronger *d*-orbital overlapping,[35] as is confirmed by the corresponding PDOS shown in Figure 2d. In both cases, the electronic modifications close to the Fermi level will induce changes in the surface reactivity, and modulate the adsorption energies of adsorbates.[36, 37]

At this point and based on the *ex situ* characterization of $Pt_{6.1}Nd$/C and $Pt_{7.8}Nd$/C, it might be expected that both electrocatalysts are particular active for the ORR. However, the observed

activity enhancement, in terms of mass activity, is only *ca*. 3-fold respect to the Pt/C benchmark. *Operando* WAXS measurements were carried out to follow any modification of the electrocatalyst structure during the electrochemical operating conditions. Conventional thin-film electrodes (20 μg_{Pt} cm^{-2}_{geo}) on glassy carbon substrates were mounted in a dedicated X-ray-transparent electrochemical flow cell described in a previous contribution[26] filled with N_2-saturated 0.1 M $HClO_4$ electrolyte and kept at the open circuit potential (OCP) prior to any measurement (see Supplementary Information S4 for more details). The electrochemical test protocol started with electrode preconditioning (or electrochemical activation) procedure, consisting of potential cycling between 0.05 and 0.95 V_{RHE} at 100 mV s^{-1} for 20 cycles. WAXS patterns were collected with 1 s temporal resolution. For both $Pt_{6.1}Nd/C$ and $Pt_{7.8}Nd/C$ electrocatalysts, significant structural changes were observed even upon the early electrochemical activation, which are shown in Figures 3 and 4, respectively.

In the case of $Pt_{6.1}Nd/C$, Figures 3a-b show that the first cathodic scan (from the OCP to 0.05 V_{RHE}) triggers the sudden growth of a pure Pt FCC phase. This crystalline phase (initially absent from the pristine sample) further evolves as soon as the electrode potential passes below 0.32 V_{RHE} (Figure 3b) and reaches a stable weight fraction of *ca.* 20 *wt.%* after only one second. For $Pt_{7.8}Nd/C$, Figures 4a-b show that, during the first cathodic scan, the pure Pt FCC phase (already present in the pristine sample) further increases once the electrode potential passes below 0.80 V_{RHE} and reaches a stable weight fraction of *ca.* 65 *wt.%* after *ca.* 10 seconds. The Pt_2Nd cubic phase that was detected in the pristine $Pt_{7.8}Nd/C$ sample was not observed *operando*, but rather an increased fraction of the Pt FCC instead. This suggests the Pt_2Nd phase converted to Pt FCC during the hold of the electrode at OCP (*ca.* 20 min during cell alignment with the X-ray beam),

highlighting the low stability of the Pt_2Nd crystalline structure under the electrochemical conditions.

For both samples, the origin of the Pt atoms constituting the growing Pt FCC phase might be correlated with the evolution of the individual phase intensities or scale factors (Figure 3c and 4c). However, the appearance of the Pt FCC phase is not correlated to the change in the intensity of Pt_5Nd, which suggests that the origin of the Pt FCC comes from the electrochemical reduction of an amorphous phase containing Pt (*e.g.*, amorphous Pt oxides). The slight decrease of the Pt_5Nd phase intensity during the subsequent electrochemical activation suggests, in both cases, possible phase conversion from the hexagonal Pt_5Nd to Pt FCC, but only to a minor extent.

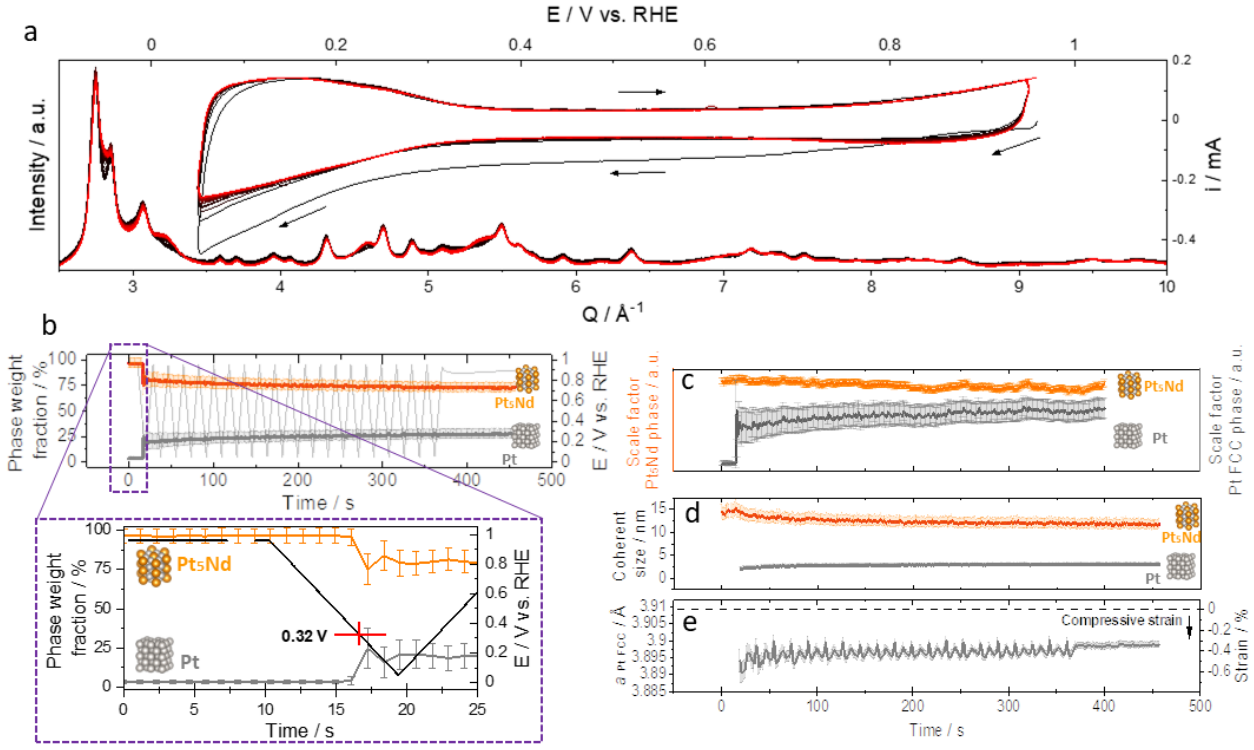

Figure 3. *Operando* WAXS analysis during the electrochemical activation of $Pt_{6.1}Nd/C$: (a) cyclic voltammogram and *operando* WAXS patterns (the arrows indicate the polarization direction); and refined microstructural parameters extracted from the WAXS patterns: (b) phase weight fractions, (c) scale factors, (d) coherent domain sizes, and (e) lattice parameter and relative strain.

For $Pt_{6.1}Nd/C$, further analysis reveals that the average coherent domain size of the Pt_5Nd phase decreases from 15 nm to 10 nm at the end of the electrochemical activation, and that the coherent domain size of the Pt FCC phase increases to *ca.* 3 nm, Figure 3d. This behaviour is consistent both with the partial phase transition from Pt_5Nd to Pt FCC triggering the formation of thicker Pt overlayers, and/or small pure Pt NPs are formed. The computed phase diagram (see the Supplementary Information S9) predicts that Pt multilayer deposits on the Pt_5Nd phase could remain kinetically stable as slow Pt diffusion should impair the nucleation of pure Pt NPs. Otherwise, the multilayer deposits could nucleate into pure Pt NPs. For $Pt_{7.8}Nd/C$, the results of Figure 4d indicate that during the electrochemical activation the average coherent domain size of the Pt_5Nd phase seems almost constant (*ca.* 3 nm), however, the coherent domain size of the Pt FCC phase seems to increase from *ca*. 3 nm to *ca.* 5 nm. This increase in size might also be related to the conversion of Pt_2Nd to Pt FCC.

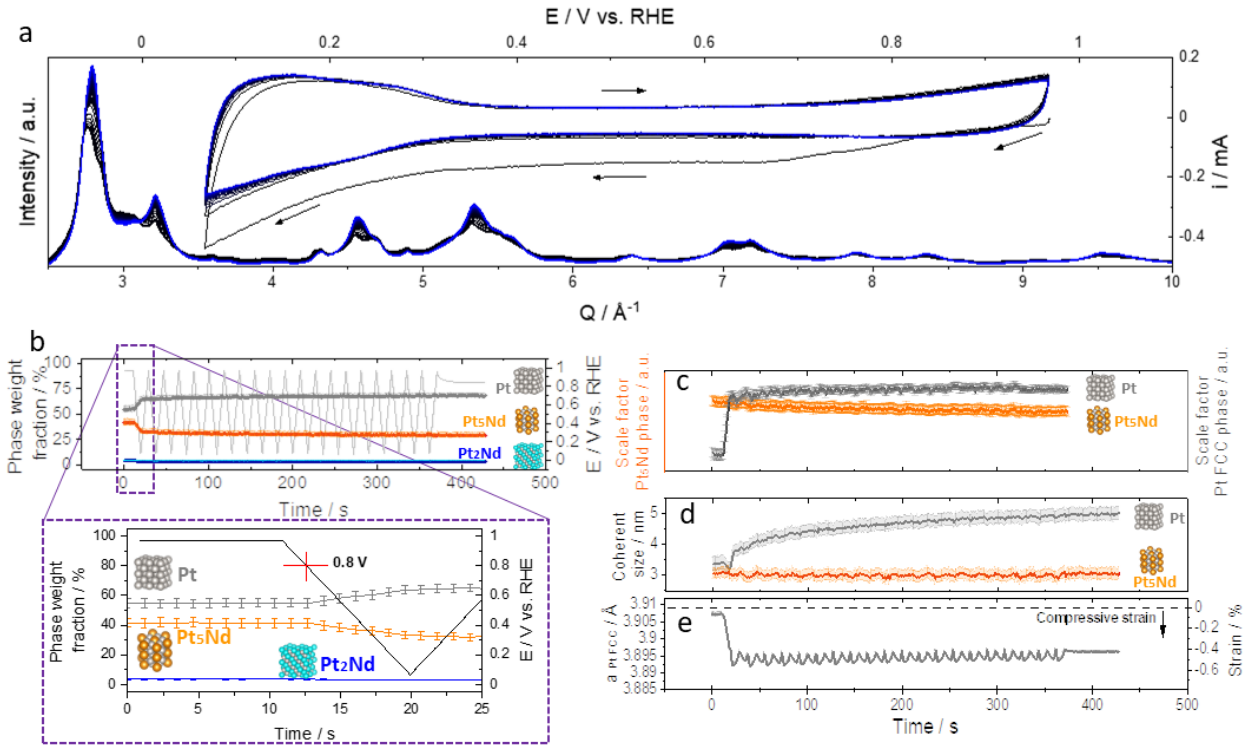

Figure 4. *Operando* WAXS analysis during the electrochemical activation of $Pt_{7.8}Nd/C$: (a) cyclic voltammogram and *operando* WAXS patterns (the arrows indicate the polarization direction); and refined microstructural parameters extracted from the WAXS patterns: (b) phase weight fractions, (c) scale factors, (d) coherent domain sizes, and (e) lattice parameter and relative strain.

For both electrocatalysts, the refined average lattice parameter of the Pt FCC phase, a_{PtFCC}, is smaller relative to the reference Pt/C (dashed black line in Figures 3e and 4e), indicating that this crystalline phase is under compressive strain. The compressive strain in both cases reaches *ca.* -0.4 % at the end of the electrochemical activation. Notwithstanding, the *operando* average strain is significantly lower than that measured *ex situ*. The model derived from DFT proposes that as the Pt shell thickness increases (higher number of Pt layers over the Pt_5Nd structure) the Pt-Pt interatomic distances through the *z*-axis increase (lattice dilation, see Figure S11 in the Supplementary Information S9), while the surface Pt atoms experience lateral compressive strain

along the *x*-*y* plane. The average residual strain is approximately -0.89 %, suggesting a counterbalance between compressive and tensile strain.

The structural evolution of the Pt_xNd/C electrocatalysts was followed through an accelerated degradation test (ADT), *c.f.* Figure 5, that used 5,000 square-wave potential cycles between 0.6-0.95 V_{RHE}[38] (see the Figure S1 in the Supplementary Information S3). The ADT was carried out under both N_2- and O_2- saturated 0.1 M $HClO_4$, although no significant structural difference was observed for catalysts aged in these different atmospheres over 5,000 cycles.

For $Pt_{6.1}Nd/C$, the phase weight fraction of the Pt_5Nd alloy decreases slightly from *ca.* 75 % to 70 % after 5,000 cycles, and the FCC Pt phase weight fraction increases from *ca.* 25 % to 30 % after the ADT. The most pronounced phase transitions take place during the first 500 electrochemical cycles, little further modification occurring thereafter. The average coherent domain size of the Pt FCC phase grew during the ADT from *ca.* 3 nm to 3.25 nm The a_{PtFCC} is shorter respect to the Pt reference during the ADT, pointing out a compressive strain, which is gently relaxed at the end of the ADT. The HAADF-STEM micrographs and the EELS chemical profiles after the ADT, *c.f.* Figure 5c and Supplementary Information S10, indicate the predominance of dense NPs, the chemical composition of which comprises both Pt and Nd. Even though the thickening of the Pt overlayer might be expected, this feature does not fully explain the increase of the average Pt FCC phase weight fraction nor its increased average coherent domain size. If we assume the presence of solid NPs with a Pt-rich overlayer thickness of 1 nm (~ 5 Pt atomic layers, see below), the remaining contribution of the Pt FCC is probably related to the presence of pure Pt NPs.

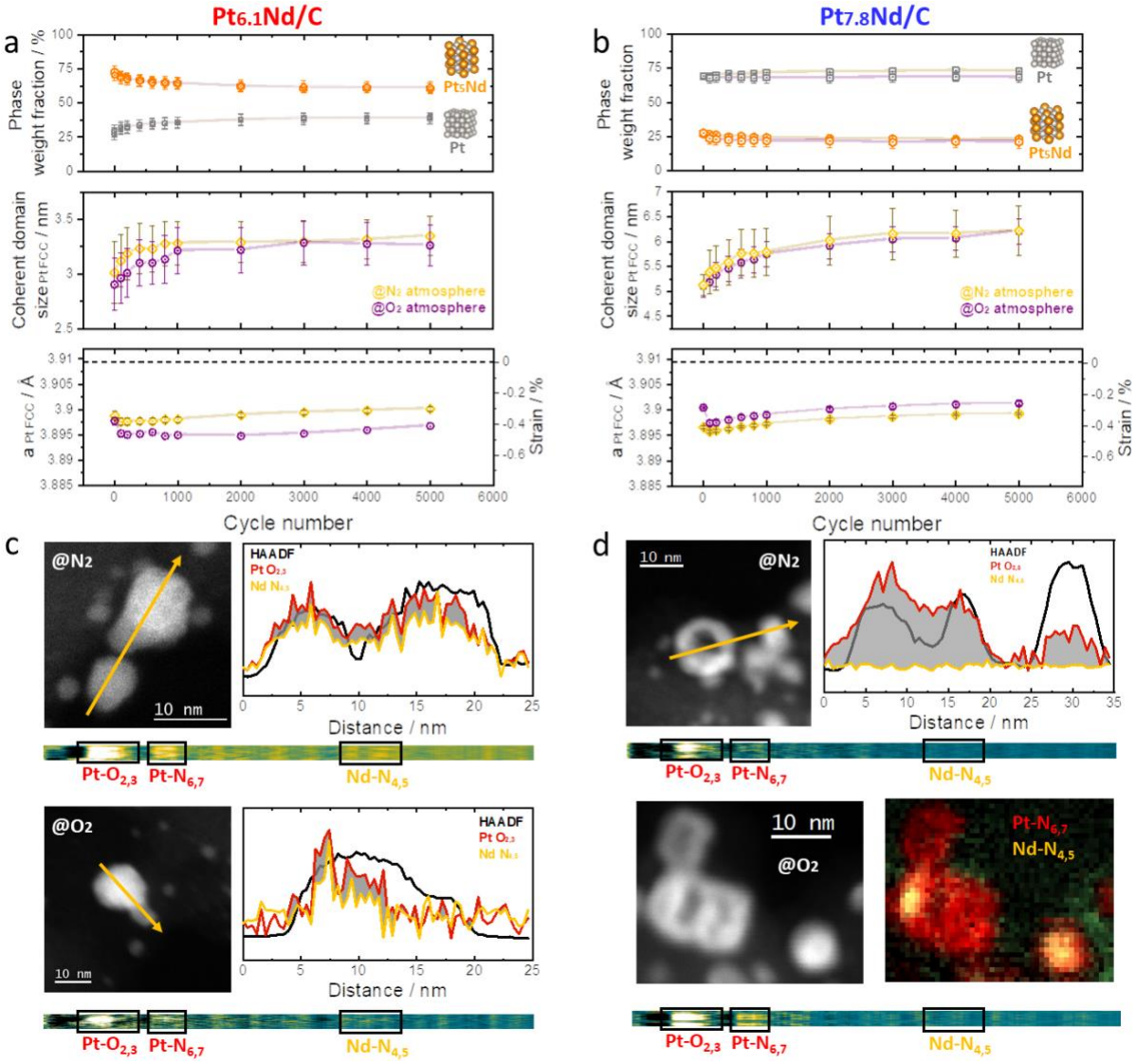

Figure 5. Refined WAXS parameters (weight fraction, coherent domain size, lattice parameter and relative strain) of the crystalline phases detected during the applied ADT of (a) $Pt_{6.1}Nd/C$ and (b) $Pt_{7.8}Nd/C$. Representative STEM/EELS chemical mapping of (d) $Pt_{6.1}Nd/C$ and (c) $Pt_{7.8}Nd/C$ after the ADT.

In contrast, in the case of $Pt_{7.8}Nd/C$, the Pt FCC phase is clearly predominant (*ca.* 75 %*wt.*) relative to the Pt_5Nd alloy (*ca.* 25 %*wt.*). This behaviour is constant along the whole ADT. The average

coherent domain size of the Pt FCC phase, indeed, increases with the cycle number, indicating the formation of bigger Pt crystalline domains during the ADT, from ~ 5 nm to ~ 6.5 nm. At the end of the ADT, the trend follows an upward behaviour, suggesting the continuous increment of the Pt crystalline domains. Meanwhile, the lattice parameter a_{PtFCC} indicates a trend towards lattice relaxation as the cycle number increases. The STEM micrographs and the EELS chemical profiles after the ADT shown in Figure 5d and Supplementary Information S10 reveal the predominance of hollow Pt structures, these architectures corresponding to the dominant Pt FCC phase. Clearly, the growing coherent domain size trend testifies to the loss of the Pt-Nd alloy, and the stabilization of Pt hollow architectures. Interestingly, the EELS mapping shown in Figure 5d (ADT@O_2) reveals the presence of solid core/shell NPs with a Pt-rich shell of *ca.* 1 nm thick (~ 5 Pt atomic layers, see Supplementary Information S10), and some domains of the hollow structures maintained the Pt-Nd alloy, supporting the *operando* WAXS results.

In addition to the structure/morphological evolution in the Pt-Nd electrocatalysts, the electrochemical strain dynamics were followed throughout the ADT, see Figure 6a and b. It has been reported that the origin of the electrochemical strain dynamics in NPs comes from the adsorption processes that take place at the electrode/electrolyte interphase,[26] whereby the adsorption/desorption events induce NP lattice expansion/contraction at the electrochemical interphase. For the Pt/C benchmark (black profile in Figure 6a and b), in the potential range of $0.05 \leq E \leq 0.30$ V_{RHE}, the hydrogen underpotential deposition (H_{upd}) region (denoted as Pt-H in Figure 6a and b), one can appreciate a reversible lattice expansion, *i.e.*, no hysteresis. In contrast, at $E > 0.5$ V_{RHE}, *i.e.*, the oxygenated species adsorption/desorption region (denoted as Pt-O in Figure 6a and b), the pronounced hysteresis indicates an irreversible structural change due to the

Pt oxidation dynamics.[39] The results of Figure 6a indicate that, strikingly, the lattice expansion is attenuated in both the Pt-H and Pt-O regions for $Pt_{6.1}Nd/C$ *vs.* the Pt/C reference, in agreement with a lower H and OH surface coverage, respectively, evoking weaker adsorption energy of both species. This tendency is maintained at the end of the ADT, so confirming by *operando* measurements the benefit of the Pt-Nd alloy. For $Pt_{7.8}Nd/C$, even though the strain dynamics in the Pt-H region are Pt-like, it seems that there is lower oxide surface coverage, relative to Pt/C, and less intense hysteresis at the Pt-O region is observed. Although the Pt-like behaviour might be explained by the presence of pure Pt architectures, the lower hysteresis (related to the oxide dynamics) in this electrocatalyst could also be linked to an effect on the local morphology, decreasing its local oxophilicity.

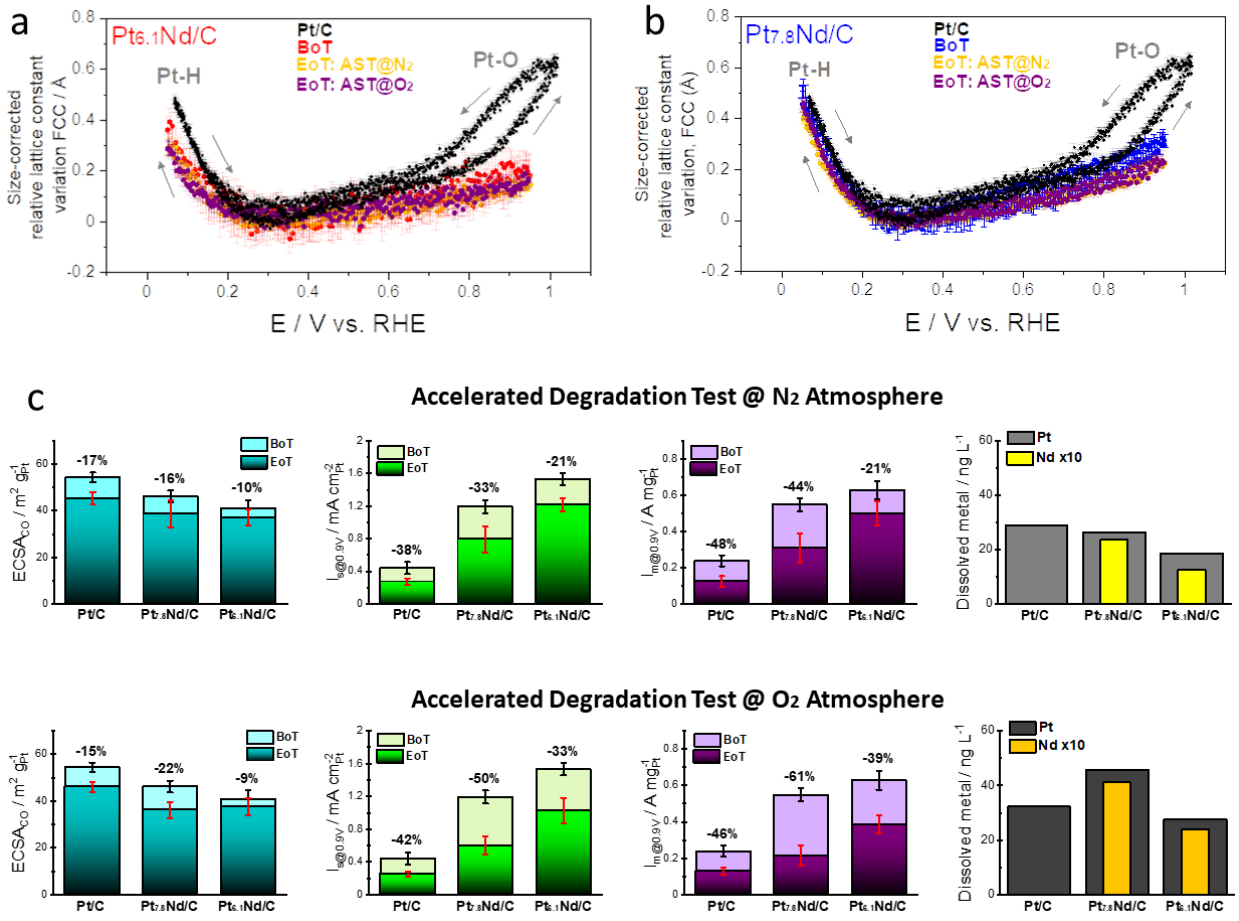

Figure 6. Potential-dependency of the relative lattice constant variation of (a) $Pt_{6.1}Nd/C$ and (b) $Pt_{7.8}Nd/C$. (c) Electrochemical active surface area (ECSA, determined by CO-stripping), specific surface activity (I_s), mass activity (I_m) and detected dissolved Pt and Nd in the electrolyte, at the beginning (BoT) and at the end (EoT) of the 30,00 cycles ADT under nitrogen or oxygen atmosphere of $Pt_{6.1}Nd/C$ and $Pt_{7.8}Nd/C$. Pt/C is used as reference.

Enhanced kinetics of the sluggish ORR in acidic medium require the binding energies (ΔE) of the key reaction intermediates, *i.e.*, O* and OH*, to be weaker than with Pt (111) by ~0.2 eV and ~0.1 eV, respectively.[40] The DFT computations performed in this work predict a weaker adsorption energy change, ΔE_{O*} and ΔE_{OH*}, of 0.248 and 0.063 eV *vs.* Pt (111), respectively, using the Pt_5Nd@5-Pt structure (this model matches better the *operando* experimental results). It

may be inferred that the enhanced adsorption properties shown in Figure 6 come from the surface compressive strain rather than the strong Pt-Nd charge transfer, since this electronic perturbation does not go beyond the two first Pt layers. In this work, the DFT results aim at guiding the interpretation of experimental observations rather than strictly predicting the behavior of the complex practical system.

The electrochemical activity-stability towards the ORR of the Pt_xNd/C electrocatalysts was evaluated using the RDE technique in 0.1 M $HClO_4$ electrolyte. The ADT consisted of 30,000 square-wave potential cycles between 0.6-0.95 V_{RHE}[38] (see the Figure S1 in the Supplementary Information S3). To visualize the possible oxygen adsorption-induced segregation effects, the ADT was carried out in N_2- and O_2-saturated electrolyte, when notable performance differences were observed after 30,000 cycles. The cyclic voltammograms in N_2-saturated 0.1 M $HClO_4$, at the beginning (BoT) and at the end (EoT) of the ADT of Figure S15 in the Supplementary Information S11 display the features typical of Pt in acidic medium. While the cyclic voltammograms of $Pt_{6.1}Nd/C$, at BoT and EoT, are characterized by a distorted H_{upd} region due to the modified Pt-H interaction on Pt-REM alloys,[13] the cyclic voltammograms of $Pt_{7.8}Nd/C$ present an intermediate Pt/Pt-alloy behaviour, in full agreement with the results discussed above.

As was mentioned above, in terms of specific ORR activity (Is), the results of Figure 6c confirm that the synthesized Pt-Nd electrocatalysts are intrinsically more active than the Pt/C benchmark, as improvement factors at BoT of 2.7 ($Pt_{7.8}Nd/C$) and 3.4 ($Pt_{6.1}Nd/C$) are observed. These features might be directly related to the enhanced adsorption properties shown in Figure 6a and b. Nonetheless, the ORR polarization curves shown in Figure S15 in the Supplementary Information

S11 reveal evident degradation after the ADT and highlight a stronger activity loss after the ADT under O_2 atmosphere. This behavior is reflected in the mass-transport-corrected ORR polarization curves (normalized by Pt mass, Figure S16 in the Supplementary Information S11), demonstrating that $Pt_{7.8}Nd/C$ and $Pt_{6.1}Nd/C$ experienced stronger degradation after the ADT under O_2 atmosphere. *Ex situ* ICP-MS measurements of the electrolyte at EoT corroborate these conclusions since higher concentration of dissolved metal was detected after electrochemical cycling in O_2 atmosphere, suggesting higher metal dissolution under these conditions. Although we have shown indirect evidence of the metal dissolution through the ADT, this *ex situ* approach is insufficiently precise, since it is not possible to disentangle the transient dissolution events that take place or quantify the metal dissolution. The ECSA, I_s and I_m values, at the BoT and EoT under both atmospheres, are exposed in Figure 6c and Table 2, with the concentration of dissolved Pt and Nd in the electrolyte.

Table 2. Electrochemical kinetic parameters of $Pt_{6.1}Nd/C$ and $Pt_{7.8}Nd/C$ at BoT and EoT. Commercial Pt/C is used as reference.

	Condition	[a] ECSA ($m^2\ g_{Pt}^{-1}$)	$I_{s@0.9\ V}$ ($mA\ cm_{Pt}^{-2}$)	$I_{m@0.9\ V}$ ($A\ mg_{Pt}^{-1}$)	[b] Dissolved metal ($ng\ L^{-1}$)
$Pt_{7.8}Nd/C$	BoT	46.19 ± 2.5	1.19 ± 0.08	0.54 ± 0.04	--
	EoT@N_2	38.85 ± 2.7	0.79 ± 0.15	0.31 ± 0.08	Pt: 26.4; Nd: 235.4
	EoT@O_2	36.17 ± 3.5	0.59 ± 0.11	0.21 ± 0.05	Pt: 45.8; Nd: 411.3
$Pt_{6.1}Nd/C$	BoT	41.00 ± 3.6	1.53 ± 0.07	0.62 ± 0.05	--
	EoT@N_2	37.01 ± 3.4	1.21 ± 0.08	0.49 ± 0.06	Pt: 18.5; Nd: 127.1
	EoT@O_2	37.59 ± 3.7	1.02 ± 0.15	0.38 ± 0.05	Pt: 27.6; Nd: 240.6
	BoT	54.41 ± 2.1	0.44 ± 0.07	0.23 ± 0.03	--

Pt/C	EoT@N_2	45.30 ± 2.7	0.27 ± 0.04	0.12 ± 0.03	Pt: 28.7
	EoT@O_2	46.02 ± 2.0	0.26 ± 0.03	0.13 ± 0.02	Pt: 32.3

a: Determined by CO-stripping; b: Determined by ICP-MS on the electrolyte recovered at EoT.

From Figure 6c and Table 2 it is concluded that the Pt/C benchmark suffered similar degradation after the ADT under both atmospheres. However, it seems that the degradation of $Pt_{7.8}Nd/C$ and $Pt_{6.1}Nd/C$ is more pronounced after the ADT under O_2 atmosphere. The ECSA variations might be related to the slight particle size changes and morphological transitions provided in the Supplementary Information S11; meanwhile, the activity attenuation of the Pt-Nd electrocatalysts is related to their compositional segregation, and decrease of the kinetic benefit from the alloying effect.

Theoretical works have suggested that in Pt-based alloys the presence of adsorbed oxygen induces segregation of the non-precious metal to the surface .[41] In fact, due to the larger atomic radii and lower surface energy of REMs relative to Pt, it is expected that the Nd atom tends to segregate to the surface. To obtain insights concerning oxygen-induced segregation of Nd in Pt-Nd alloys, we have performed DFT calculations of the segregation energies (E_{seg}) of the Nd atom on the Pt (111) surface in the presence and absence of oxygen. Figure S20 in the Supplementary Information S12 illustrates how the E_{seg} of one Nd atom evolves as a function of its position in the Pt slab in the presence and in the absence of adsorbed oxygen, revealing the strong oxygen-induced segregation of Nd towards the topmost surface layer of Pt (the more negative E_{seg} value, the greater the segregation). The segregation energy of a Nd atom located on the first surface layer interacting with oxygen is more than double that in the absence of oxygen (E_{seg} = -4.7 eV *vs.* -2.1 eV).

Furthermore, the effect of oxygen seems to be limited to the Nd atoms located in the two top layers; the Nd atoms located in the third and fourth layers are found to have a bulk-like behaviour and the presence of oxygen does not induce their segregation. This result is in line with the reported isosurfaces in Pt_5Nd@5-Pt, suggesting the strong segregation of Nd atoms located in the upper surface layers and their dissolution during the ADT under oxygen atmosphere, resulting in Pt-Nd alloy system with constrained Pt outer surface layers.

4. CONCLUSION

The $Pt_{6.1}Nd$ composition has the highest ORR activity among the carbon-supported Pt-Nd nanoalloy series. Even though the *ex situ* characterization techniques revealed surface compressive strain and electronic modifications due to the strong charge transfer between Pt and Nd, at the electrochemical operating conditions, the structure of the electrocatalysts underwent significant transformation. The strongest of these were observed during the early electrode conditioning (electrochemical surface activation) rather than through ADT of 5,000 cycles. The *operando* determined electrochemical strain dynamics and DFT predictions provided evidence for enhanced adsorption properties of $Pt_{6.1}Nd/C$ before and after the electrochemical cycling, which are reflected in the ORR activity in the RDE. No significant structural changes were detected during the 5,000 cycles ADT under inert (N_2) or reactive (O_2) atmosphere. However, after a 30,000 cycle ADT, the O_2 atmosphere induces higher electrocatalytic activity decay relative to that observed under N_2 atmosphere. This behaviour is consistent with Nd segregation induced by oxygen adsorption, and diminished ORR kinetic benefit from the Pt-Nd alloy. Even though the expected high activity/stability on this Pt-REM/C nanoalloys was not observed, the *operando* structure-activity-

stability relations described underpin further optimization/understanding of carbon-supported Pt-rare earth nanoalloys as fuel cell cathode catalysts.

This study is a contribution to the understanding of the structure-activity-stability relationships of carbon-supported Pt-rare earth nanoalloys under electrochemical conditions.

AUTHOR INFORMATION

Corresponding Author

**Sara Cavaliere*

Email: Sara.Cavaliere@umontpellier.fr

ORCID

C.A. Campos-Roldán: 0000-0002-1517-9037

R. Chattot: 0000-0001-6169-530X

J.S. Filhol: 0000-0002-3681-9267

H. Guesmi : 0000-0002-9369-523X

F. Pailloux: 0000-0002-9217-4723

P.-Y. Blanchard: 0000-0003-1659-6868

A. Zitolo : 0000-0002-2187-6699

D. Jones: 0000-0003-3787-2462

S. Cavaliere: 0000-0003-0939-108X

Author Contributions

The manuscript was written through contributions of all authors. All authors have given approval to the final version of the manuscript.

Author Contributions

Carlos A. Campos-Roldán : Writing-original draft, conceptualization, formal analysis, investigation, **Raphaël Chattot** : Writing-review & editing, conceptualization, formal analysis, investigation, **Jean-Sébastien Filhol** : Writing-review & editing, formal analysis, methodology, **Hazar Guesmi** : Writing-review & editing, formal analysis, methodology, **Frédéric Pailloux** : Writing-review & editing, formal analysis, investigation, **Rémi Bacabe** : Investigation, **Pierre-Yves Blanchard** : Writing-review & editing, supervision, **Andrea Zitolo** : Writing-review & editing, formal analysis, investigation, **Jakub Drnec** : Writing-review & editing, formal analysis, investigation, **Deborah J. Jones** : Writing-review & editing, conceptualization, funding acquisition, supervision, **Sara Cavaliere** : Writing-review & editing, conceptualization, funding acquisition, supervision

ASSOCIATED CONTENT

The following files are available free of charge.

Supporting Information: Experimental methodology, electrocatalysts optimization and selection, supplementary spectroscopy information, phase stability diagram, characterization after the ADT, and oxygen-induced segregation diagram.are available in the Supporting Information.

ACKNOWLEDGEMENTS

The research leading to these results has received funding from the IMMORTAL project, which receives funding from the Fuel Cells and Hydrogen 2 Joint Undertaking (now Clean Hydrogen Partnership) under grant agreement No 101006641. This Joint Undertaking receives support from the European Union's Horizon 2020 research and innovation programme, Hydrogen Europe and Hydrogen Europe Research. We acknowledge the European Synchrotron Radiation Facility (ESFR) for provision of synchrotron radiation facilities at the ID31 beamline (DOI 10.15151/ESFR-ES-673897258). We also acknowledge Synchrotron SOLEIL (Gif-sur Yvette, France) for provision of synchrotron radiation facilities at beamline SAMBA.

REFERENCES

1. van der Spek, M.; Banet, C.; Bauer, C.; Gabrielli, P.; Goldthorpe, W.; Mazzotti, M.; Munkejord, S. T.; Røkke, N. A.; Shah, N.; Sunny, N.; Sutter, D.; Trusler, J. M.; Gazzani, M., Perspective on the hydrogen economy as a pathway to reach net-zero CO_2 emissions in Europe. *Energy Environ. Sci.* **2022,** *15* (3), 1034-1077.
2. Cullen, D. A.; Neyerlin, K. C.; Ahluwalia, R. K.; Mukundan, R.; More, K. L.; Borup, R. L.; Weber, A. Z.; Myers, D. J.; Kusoglu, A., New roads and challenges for fuel cells in heavy-duty transportation. *Nat. Energy* **2021,** *6* (5), 462-474.
3. Kodama, K.; Nagai, T.; Kuwaki, A.; Jinnouchi, R.; Morimoto, Y., Challenges in applying highly active Pt-based nanostructured catalysts for oxygen reduction reactions to fuel cell vehicles. *Nat Nanotechnol* **2021,** *16* (2), 140-147.
4. Jiao, K.; Xuan, J.; Du, Q.; Bao, Z.; Xie, B.; Wang, B.; Zhao, Y.; Fan, L.; Wang, H.; Hou, Z.; Huo, S.; Brandon, N. P.; Yin, Y.; Guiver, M. D., Designing the next generation of proton-exchange membrane fuel cells. *Nature* **2021,** *595* (7867), 361-369.
5. Ahn, C. Y.; Park, J. E.; Kim, S.; Kim, O. H.; Hwang, W.; Her, M.; Kang, S. Y.; Park, S.; Kwon, O. J.; Park, H. S.; Cho, Y. H.; Sung, Y. E., Differences in the Electrochemical Performance of Pt-Based Catalysts Used for Polymer Electrolyte Membrane Fuel Cells in Liquid Half- and Full-Cells. *Chem Rev* **2021,** *121* (24), 15075-15140.
6. Zhao, L.; Zhu, J.; Zheng, Y.; Xiao, M.; Gao, R.; Zhang, Z.; Wen, G.; Dou, H.; Deng, Y. P.; Yu, A.; Wang, Z.; Chen, Z., Materials Engineering toward Durable Electrocatalysts for Proton Exchange Membrane Fuel Cells. *Adv. Energy Mater.* **2021,** *12* (2), 2102665.

7. Borup, R. L.; Kusoglu, A.; Neyerlin, K. C.; Mukundan, R.; Ahluwalia, R. K.; Cullen, D. A.; More, K. L.; Weber, A. Z.; Myers, D. J., Recent developments in catalyst-related PEM fuel cell durability. *Curr Opin Electrochem* **2020,** *21*, 192-200.
8. Greeley, J.; Stephens, I. E.; Bondarenko, A. S.; Johansson, T. P.; Hansen, H. A.; Jaramillo, T. F.; Rossmeisl, J.; Chorkendorff, I.; Norskov, J. K., Alloys of platinum and early transition metals as oxygen reduction electrocatalysts. *Nat Chem* **2009,** *1* (7), 552-6.
9. Vej-Hansen, U. G.; Rossmeisl, J.; Stephens, I. E.; Schiotz, J., Correlation between diffusion barriers and alloying energy in binary alloys. *Phys Chem Chem Phys* **2016,** *18* (4), 3302-7.
10. Stephens, I. E. L.; Bondarenko, A. S.; Bech, L.; Chorkendorff, I., Oxygen Electroreduction Activity and X-Ray Photoelectron Spectroscopy of Platinum and Early Transition Metal Alloys. *ChemCatChem* **2012,** *4* (3), 341-349.
11. Escudero-Escribano, M.; Verdaguer-Casadevall, A.; Malacrida, P.; Gronbjerg, U.; Knudsen, B. P.; Jepsen, A. K.; Rossmeisl, J.; Stephens, I. E.; Chorkendorff, I., Pt_5Gd as a highly active and stable catalyst for oxygen electroreduction. *J Am Chem Soc* **2012,** *134* (40), 16476-9.
12. Malacrida, P.; Escudero-Escribano, M.; Verdaguer-Casadevall, A.; Stephens, I. E. L.; Chorkendorff, I., Enhanced activity and stability of Pt–La and Pt–Ce alloys for oxygen electroreduction: the elucidation of the active surface phase. *J. Mater. Chem. A* **2014,** *2* (12), 4234-4243.
13. Escudero-Escribano, M.; Malacrida, P.; Hansen, M.; Vej-Hansen, U.; Velázquez-Palenzuela, A.; Tripkovic, V.; Schiøtz, J.; Rossmeisl, J.; Stephens, I.; Chorkendorff, I., Tuning the activity of Pt alloy electrocatalysts by means of the lanthanide contraction. *Science* **2016,** *352* (6281), 73-76.
14. Hernandez-Fernandez, P.; Masini, F.; McCarthy, D. N.; Strebel, C. E.; Friebel, D.; Deiana, D.; Malacrida, P.; Nierhoff, A.; Bodin, A.; Wise, A. M.; Nielsen, J. H.; Hansen, T. W.; Nilsson, A.; Stephens, I. E.; Chorkendorff, I., Mass-selected nanoparticles of Pt_xY as model catalysts for oxygen electroreduction. *Nat Chem* **2014,** *6* (8), 732-8.
15. Velázquez-Palenzuela, A.; Masini, F.; Pedersen, A. F.; Escudero-Escribano, M.; Deiana, D.; Malacrida, P.; Hansen, T. W.; Friebel, D.; Nilsson, A.; Stephens, I. E. L.; Chorkendorff, I., The enhanced activity of mass-selected Pt_xGd nanoparticles for oxygen electroreduction. *J. Catal.* **2015,** *328*, 297-307.
16. Pedersen, A. F.; Ulrikkeholm, E. T.; Escudero-Escribano, M.; Johansson, T. P.; Malacrida, P.; Pedersen, C. M.; Hansen, M. H.; Jensen, K. D.; Rossmeisl, J.; Friebel, D.; Nilsson, A.; Chorkendorff, I.; Stephens, I. E. L., Probing the nanoscale structure of the catalytically active overlayer on Pt alloys with rare earths. *Nano Energy* **2016,** *29*, 249-260.
17. Hu, Y.; Jensen, J. O.; Norby, P.; Cleemann, L. N.; Yang, F.; Li, Q., Mechanistic Insights into the Synthesis of Platinum–Rare Earth Metal Nanoalloys by a Solid-State Chemical Route. *Chem. Mater.* **2021,** *33* (2), 535-546.
18. Hu, Y.; Jensen, J. O.; Cleemann, L. N.; Brandes, B. A.; Li, Q., Synthesis of Pt-Rare Earth Metal Nanoalloys. *J Am Chem Soc* **2020,** *142* (2), 953-961.
19. Kanady, J. S.; Leidinger, P.; Haas, A.; Titlbach, S.; Schunk, S.; Schierle-Arndt, K.; Crumlin, E. J.; Wu, C. H.; Alivisatos, A. P., Synthesis of Pt_3Y and Other Early-Late Intermetallic Nanoparticles by Way of a Molten Reducing Agent. *J Am Chem Soc* **2017,** *139* (16), 5672-5675.

20. Itahara, H.; Takatani, Y.; Takahashi, N.; Kosaka, S.; Nagoya, A.; Inaba, M.; Kamitaka, Y.; Morimoto, Y., Synthesis of Carbon-Supported Intermetallic Pt_5Ce Compound Nanoparticles via a Water-Based Impregnation Route. *Chem. Mater.* **2021,** *34* (1), 422-429.
21. Gunji, T.; Tanaka, S.; Inagawa, T.; Otsuka, K.; Matsumoto, F., Atomically Ordered Pt_5La Nanoparticles as Electrocatalysts for the Oxygen Reduction Reaction. *ACS Appl. Nano Mater.* **2022,** *5* (4), 4958-4965.
22. Campos-Roldán, C. A.; Jones, D. J.; Rozière, J.; Cavaliere, S., Platinum-Rare Earth Alloy Electrocatalysts for the Oxygen Reduction Reaction: A Brief Overview. *ChemCatChem* **2022,** *14* (19), e202200334.
23. Campos-Roldán, C. A.; Parnière, A.; Donzel, N.; Pailloux, F.; Blanchard, P.-Y.; Jones, D. J.; Rozière, J.; Cavaliere, S., Influence of the Carbon Support on the Properties of Platinum–Yttrium Nanoalloys for the Oxygen Reduction Reaction. *ACS Applied Energy Materials* **2022,** *5* (3), 3319-3328.
24. Timoshenko, J.; Roldan Cuenya, B., In Situ/Operando Electrocatalyst Characterization by X-ray Absorption Spectroscopy. *Chem Rev* **2021,** *121* (2), 882-961.
25. Sasaki, K.; Marinkovic, N.; Isaacs, H. S.; Adzic, R. R., Synchrotron-Based In Situ Characterization of Carbon-Supported Platinum and Platinum Monolayer Electrocatalysts. *ACS Catal.* **2015,** *6* (1), 69-76.
26. Chattot, R.; Martens, I.; Mirolo, M.; Ronovsky, M.; Russello, F.; Isern, H.; Braesch, G.; Hornberger, E.; Strasser, P.; Sibert, E.; Chatenet, M.; Honkimaki, V.; Drnec, J., Electrochemical Strain Dynamics in Noble Metal Nanocatalysts. *J Am Chem Soc* **2021,** *143* (41), 17068-17078.
27. Kawaguchi, T.; Komanicky, V.; Latyshev, V.; Cha, W.; Maxey, E. R.; Harder, R.; Ichitsubo, T.; You, H., Electrochemically Induced Strain Evolution in Pt-Ni Alloy Nanoparticles Observed by Bragg Coherent Diffraction Imaging. *Nano Lett* **2021,** *21* (14), 5945-5951.
28. Fuchs, T., Drnec, J., Calle-Vallejo, F., Stubb, N., Sandbeck, D., Ruge, M., Cherevko, S., Harrington, D., Magnussen, O., Structure dependency of the atomic-scale mechanisms of platinum electro-oxidation and dissolution. *Nat Catal* **2020,** *3*, 754-761.
29. Campos-Roldán, C. A.; Pailloux, F.; Blanchard, P.-Y.; Jones, D. J.; Rozière, J.; Cavaliere, S., Rational Design of Carbon-Supported Platinum–Gadolinium Nanoalloys for Oxygen Reduction Reaction. *ACS Catal.* **2021,** *11* (21), 13519-13529.
30. Campos-Roldan, C. A.; Pailloux, F.; Blanchard, P. Y.; Jones, D. J.; Roziere, J.; Cavaliere, S., Enhancing the activity and stability of carbon-supported platinum-gadolinium nanoalloys towards the oxygen reduction reaction. *Nanoscale Adv* **2021,** *4* (1), 26-29.
31. Gan, L.; Heggen, M.; O'Malley, R.; Theobald, B.; Strasser, P., Understanding and controlling nanoporosity formation for improving the stability of bimetallic fuel cell catalysts. *Nano Lett* **2013,** *13* (3), 1131-8.
32. Guo, Q.; Kleppa, O., Standard Enthalpies of Formation of Neodymium Alloys, Nd + Me (Me = Ni, Ru, Rh, Pd, Ir, Pt), by High-Temperature Direct Synthesis Calorimetry. *Metall. Mater. Trans. B* **1995,** *26B*, 275-279.
33. Liu, J.; Tennessen, E.; Miao, J.; Huang, Y.; Rondinelli, J.; Heinz, H., Understanding Chemical Bonding in Alloys and the Representation in Atomistic Simulations. *J. Phys. Chem. C* **2018,** *122*, 14996−15009.
34. Luo, M.; Guo, S., Strain-controlled electrocatalysis on multimetallic nanomaterials. *Nat. Rev. Mater.* **2017,** *2* (11), 17059.

35. Filhol, J. S.; Simon, D.; Sautet, P., Stress induced nanostructure in a Pd monolayer on Ni(110): a first principles theoretical study. *Surf. Sci.* **2001,** *472* (1), L139-L144.
36. Filhol, J. S.; Simon, D.; Sautet, P., Understanding the High Activity of a Nanostructured Catalyst Obtained by a Deposit of Pd on Ni: First Principle Calculations. *J. Am. Chem. Soc.* **2004,** *126* (10), 3228-3233.
37. Filhol, J. S.; Saint-Lager, M. C.; De Santis, M.; Dolle, P.; Simon, D.; Baudoing-Savois, R.; Bertolini, J. C.; Sautet, P., Highly Strained Structure of a Four-Layer Deposit of Pd on Ni(110): A Coupled Theoretical and Experimental Study. *Phys. Rev. Lett.* **2002,** *89* (14), 146106.
38. Stariha, S.; Macauley, N.; Sneed, B. T.; Langlois, D.; More, K. L.; Mukundan, R.; Borup, R. L., Recent Advances in Catalyst Accelerated Stress Tests for Polymer Electrolyte Membrane Fuel Cells. *J. Electrochem. Soc.* **2018,** *165* (7), F492-F501.
39. Martens, I.; Chattot, R.; Rasola, M.; Blanco, M. V.; Honkimäki, V.; Bizzotto, D.; Wilkinson, D. P.; Drnec, J., Probing the Dynamics of Platinum Surface Oxides in Fuel Cell Catalyst Layers Using in Situ X-ray Diffraction. *ACS Appl. Energy Mater.* **2019,** *2* (11), 7772-7780.
40. Čolić, V.; Bandarenka, A. S., Pt Alloy Electrocatalysts for the Oxygen Reduction Reaction: From Model Surfaces to Nanostructured Systems. *ACS Catal.* **2016,** *6* (8), 5378-5385.
41. Sarwar, M.; Gavartin, J. L.; Martinez Bonastre, A.; Garcia Lopez, S.; Thompsett, D.; Ball, S. C.; Krzystala, A.; Goldbeck, G.; French, S. A., Exploring fuel cell cathode materials using ab initio high throughput calculations and validation using carbon supported Pt alloy catalysts. *Phys Chem Chem Phys* **2020,** *22* (10), 5902-5914.

TOC graphic